

1 **REVISION 1**

2 **New insights into the zircon-reidite phase transition**

3 Claudia Stangarone<sup>1\*</sup>, Ross J. Angel<sup>1</sup>, Mauro Prencipe<sup>2</sup>, Boriana Mihailova<sup>3</sup>, Matteo Alvaro<sup>1</sup>

4 <sup>1</sup> *Department of Earth and Environmental Sciences, University of Pavia, Via A. Ferrata 1, I-27100 Pavia, Italy,*

5 <sup>2</sup> *Earth Sciences Department, University of Torino, Via Valperga Caluso 35, I-10125 Torino, Italy*

6 <sup>3</sup> *Department of Earth Sciences, University of Hamburg, Grindelallee 48, D-20146 Hamburg, Germany*

7 *\*Current address: Institute for Planetary Research, Deutschen Zentrums für Luft- und Raumfahrt, Rutherfordstraße 2,*

8 *D-12489 Berlin, Germany*

9

10 **Corresponding author: R.J. Angel, [ross.angel@unipv.it](mailto:ross.angel@unipv.it)**

11 **Submitted to *American Mineralogist*: 27-Sept-2018**

12 **Revised version of 8-March-2019**

13

14

**ABSTRACT**

15 The structure, the elastic properties and the Raman frequencies of the zircon and reidite polymorphs  
16 of ZrSiO<sub>4</sub> were calculated as a function of hydrostatic pressure up to 30 GPa using HF/DFT ab-initio  
17 calculations at static equilibrium (0 K). The softening of a silent (B<sub>1u</sub>) mode of zircon leads to a phase  
18 transition to a “high-pressure - low-symmetry” (HPLS) ZrSiO<sub>4</sub> polymorph with space group  $I\bar{4}2d$   
19 and cell parameters  $a=6.4512 \text{ \AA}$   $c=5.9121 \text{ \AA}$   $V = 246.05 \text{ \AA}^3$  (at 20 GPa). The primary coordination of  
20 SiO<sub>4</sub> and ZrO<sub>8</sub> groups in the structure of zircon is maintained in the high-pressure phase, and the new  
21 phase deviates from that of zircon by the rotation of SiO<sub>4</sub> tetrahedra and small distortions of the ZrO<sub>8</sub>  
22 dodecahedra. The new polymorph is stable with respect to zircon at 20 GPa and remains a  
23 dynamically-stable structure up to at least 30 GPa. On pressure release the new phase reverts back to  
24 the zircon structure, and therefore cannot be quenched in experiments. In contrast, the transformation  
25 from zircon to reidite is reconstructive in nature and results in a first-order transition with a volume  
26 and density change of about 9%. The calculated energies from the DFT simulations yield an  
27 equilibrium transition pressure of 9.13(1) GPa at 0 K. Simulations of the Raman spectra of the three

28 polymorphs at 20 GPa show how they can be distinguished. In particular, the peak due to the lowest-  
29 energy  $A_1$  mode with a calculated wavenumber of  $94\text{ cm}^{-1}$  is diagnostic of the HPLS phase because  
30 it does not overlap with any of the peaks of zircon or reidite.

31

32 **Keywords:** zircon, reidite, phase transition, Raman spectroscopy, high pressure

33

## INTRODUCTION

34 Zircon ( $\text{ZrSiO}_4$ , space group  $I4_1/amd$ ) is an extremely stiff material and upon meteorite bombardment  
35 shock microstructures form within it at pressures of 20 GPa or more (Leroux et al. 1999). These  
36 microstructures remarkably survive subsequent metamorphism without being obliterated and,  
37 therefore, they can provide diagnostic criteria to identify impact structures (French 1998; French and  
38 Koeberl 2010, Wittmann et al. 2006). During shocks zircon may transform into the high-pressure  
39 scheelite-type polymorph reidite (space group  $I4_1/a$ ). Naturally-occurring reidite was first identified  
40 using X-ray diffraction (XRD) in zircon grains from Eocene ejecta associated with the  $\sim 90$  km  
41 diameter, ca. 35.7 Ma Chesapeake Bay impact structure (Glass and Liu 2001; Glass et al. 2002) and  
42 subsequently in several other impact structures (Gucsik et al. 2004; Wittmann et al. 2006, Wittmann  
43 and Reimold 2009, Chen et al. 2013, Cavosie et al. 2015, Singleton et al. 2015, Reddy et al. 2015,  
44 Cavosie et al. 2018). Therefore, in order to study the origin of impact structures and to further  
45 constrain the impact conditions it is crucial to understand the stability relationships between zircon  
46 and its high-pressure polymorph reidite.

47 This phase transition from zircon to reidite has a volume decrease of about 9% (e.g. Reid and  
48 Ringwood 1969; Ono et al. 2004a) which suggests that it is thermodynamically first-order. Moreover,  
49 the topological differences in the atomic linkages indicate that the zircon-reidite phase transition is  
50 reconstructive, which is supported by ab initio calculations (e.g. Marqués et al. 2006, Dutta and  
51 Mandal 2012a). Because of the reconstructive nature of the zircon-reidite transformation, the  
52 equilibrium transition pressure is not well constrained. At elevated temperatures of 1000–1500 K the  
53 pressure-induced zircon-to-reidite phase transition occurs near 8 GPa (Reid and Ringwood 1969, Ono  
54 et al. 2004b). Several static loading experiments in diamond-anvil pressure cells at room temperature

55 have shown the presence of reidite when the pressure is increased above 18-23 GPa (Knittle and  
56 Williams 1993; Van Westrenen et al. 2004, Morozova 2015). However, there seems to be a  
57 discrepancy between the detection of reidite by Raman spectroscopy in the samples compressed to  
58 ca. 20 GPa and higher pressures at room temperature, and the results of X-ray diffraction which show  
59 evidence only of zircon (van Westrenen et al. 2004). On the other hand, shock wave studies found  
60 this transformation to occur at much higher pressures (30–50 GPa) (Liu 1979, Kusaba et al. 1986,  
61 Gucsik et al. 2004) and very quickly, at microsecond time scales. The latter observation favors a  
62 martensitic transformation mechanism for impact-produced reidite, since other solid-state  
63 mechanisms seem unlikely to operate on the nanosecond to seconds timescale of shock events  
64 because diffusion rates are too slow (Langenhorst and Deutsch 2012).

65 Therefore, to elucidate the pressure-induced structural transformations of zircon we have performed  
66 *ab initio* simulations of zircon and reidite to determine their structures, elastic behavior, phonon  
67 frequencies and the energy curves as a function of pressure (up to 25 GPa and 17 GPa respectively)  
68 at 0 K, which allow us to resolve the ambiguities in the experimental data. We also provide calculated  
69 Raman spectra which will aid in the identification of the polymorphs of zircon.

70

71

## METHODS

72 Ab initio HF/DFT simulations were performed with the two most recent versions of the CRYSTAL  
73 code, CRYSTAL14 (Dovesi et al., 2014) and CRYSTAL17 (Dovesi et al. 2018), employing the  
74 hybrid Hamiltonian WC1LYP which is particularly suitable for the correct reproduction of the elastic  
75 and vibrational properties of crystals (e.g. Prencipe 2012; Aliatis et al. 2015; Stangarone et al. 2016,  
76 2017). In this Hamiltonian the Wu-Cohen DFT-GGA exchange contribution (Wu and Cohen 2005)  
77 is corrected by mixing it with a percentage (16%) of the exact non-local Hartree-Fock exchange. The  
78 correlation is described by the LYP functional (Lee et al. 1988). The localized *contracted* atomic  
79 basis sets used were Si 86-311G(1d) (Pascale et al. 2004) and 8-411G(2d) (Valenzano et al. 2006)  
80 for Si and O, respectively, and the Hay–Wadt (HAYW) small-core (SC) pseudopotential basis  
81 SC\_HAYWSC-3111(32111df) (Sophia et al. 2013) for Zr. The basis sets were taken from the

82 repository at the address <http://www.crystal.unito.it/basis-sets.php>. In CRYSTAL, the level of  
83 accuracy in evaluating the Coulomb and Hartree–Fock exchange series is controlled by five  
84 parameters (Dovesi et al. 2018), specified by the TOLINTEG keyword in CRYSTAL. These  
85 parameters were set to 8, 8, 8, 8, and 18. Reciprocal space was sampled using a regular sublattice  
86 with a shrinking factor of 4, corresponding to 24 independent  $k$  vectors in the irreducible part of the  
87 Brillouin zone. The exchange–correlation DFT contributions to the Fock matrix were evaluated by  
88 numerical integration over the unit cell volume. Radial and angular points for the integration grid  
89 were generated through Gauss–Legendre radial quadrature and Lebedev two-dimensional angular  
90 point distributions. In the present work, a pruned grid with 75 radial and 974 angular points was used  
91 (see XLGRID keyword in the CRYSTAL manual). Such parameters defined grids of 17604 points in  
92 the unit cell for zircon, and 32094 for reidite. A measure of the high numerical accuracy reached with  
93 the grids is the evaluation of the total number of electrons in the unit cell, by the numerical integration  
94 of the electron density over the cell volume. For zircon we obtained 116.00003 electrons and for  
95 reidite 116.00013, both out of 116, for the reference static volume (0 K, with no zero-point vibrational  
96 effects included) at 0 GPa. The crystal structures were optimized on the basis of analytical energy  
97 gradients with respect to fractional atomic coordinates and unit cell parameters (Doll 2001, Civalleri  
98 et al. 2001). Default values were chosen for convergence of gradient components as well as nuclear  
99 displacements. For the optimized crystallographic structure, the calculation of all phonon modes in  
100 zircon was carried out at static equilibrium. Vibrational wavenumbers and normal modes were  
101 calculated within the limit of the harmonic approximation, by diagonalizing a mass-weighted Hessian  
102 matrix, whose elements are the second derivatives of the full potential of the crystal with respect to  
103 mass weighted atomic displacements. The first derivatives of the energy with respect to the atomic  
104 positions are calculated analytically (Doll et al. 2001), whereas the second derivatives are numerically  
105 calculated by setting the nuclear displacements to 0.003 Å from the equilibrium positions. The  
106 phonon frequencies and the structural data (atom coordinates and unit-cell parameters) are reported  
107 in the deposited *crystallographic information files (CIFs)*. Relative Raman intensities were computed  
108 using a fully analytical approach (Maschio et al. 2013) implemented in the CRYSTAL14 program. It

109 combines analytical gradients (Doll et al. 2001) with solutions of first-order and second-order coupled  
110 perturbed Hartree–Fock/Kohn–Sham equations (Ferrero et al. 2008) for the linear and quadratic  
111 orbital responses to electric fields in the different Cartesian directions. The thresholds for  
112 convergence of the coupled perturbed equations were set to the default values (Dovesi et al. 2014).  
113 Simulations were performed at 10 pressures from 0 to 25 GPa for zircon and 8 pressures to 17 GPa  
114 for reidite. The  $P$ - $V$  equations of state have been computed from these data with both CRYSTAL17,  
115 by using the fully-automated scheme (option EOS), or with CRYSTAL14 by fitting the unit-cell  
116 volumes and pressures from the simulations with EosFit7c (Angel et al. 2014). Both methods yield  
117 the same results within numerical rounding errors.

118

## 119 RESULTS AND DISCUSSION

120

### 121 Zircon Structure

122 The structure of zircon contains Si in tetrahedral coordination by oxygen, and Zr in 8-fold  
123 coordination by oxygen in the form of a triangular-faced dodecahedron (sometimes called a sub-  
124 disphenoid). Four of the 18 edges of each of the  $ZrO_8$  polyhedra are shared with neighboring  $ZrO_8$   
125 polyhedra to form a 3-dimensional framework (Figure 1a). A further two edges are shared with two  
126  $SiO_4$  tetrahedra to form chains of alternating edge-shared  $SiO_4$  and  $ZrO_8$  polyhedra that run along the  
127  $c$ -axis. The remaining four edges of the  $SiO_4$  tetrahedra are unshared and the  $SiO_4$  tetrahedra are  
128 isolated from one another.

129 The optimized structure of zircon obtained from the DFT simulation at static conditions (0 K, with  
130 no zero point vibrational effects included) and zero pressure exhibits unit-cell parameters that are  
131 about 0.6% larger than recent experimental values at room conditions (Finch et al., 2001, Kolesov et  
132 al. 2001, Finch and Hanchar 2003) and the Si-O bonds and the shorter Zr-O bonds (around 2.15 Å)  
133 in the simulation are both about 0.7-0.8% longer than the experimentally-determined values. This  
134 behavior is expected when GGA functionals are employed, and is probably due to the self-interaction  
135 error (Cremer 2001) as the overestimation of the volume of the core region where the electron

136 correlation is large (due to the high electron density) is not perfectly corrected by the DFT functionals.  
137 However, since the core region plays no role in determining chemical properties of the system, this  
138 is not a problem. What is important for studying the phase transformation of zircon to reidite, which  
139 have the same primary coordination of Si and Zr, is that the local structural distortions in zircon are  
140 well-reproduced by the DFT simulation. Thus, the Zr-O bonds to the shared dodecahedral O-O edges  
141 with the SiO<sub>4</sub> tetrahedra are 0.13 Å longer than those to O not involved in edge-sharing with the SiO<sub>4</sub>,  
142 and the O-Si-O angle to the same shared edge is only 96.5° (Figure 2), which are within 2 esd's of the  
143 experimental values at room conditions (Finch et al., 2001, Kolesov et al. 2001).

144

#### 145 **Zircon under hydrostatic pressure**

146 The simulation at 5 GPa, and the changes from the simulation at zero pressure (both at 0 K), show  
147 the same approximately uniform compression of the structure reported in the only (to the authors'  
148 knowledge) experimental high-pressure structural study of zircon (Hazen and Finger 1979) which  
149 was limited to a maximum pressure of 4.8 GPa. The higher precision of the DFT simulations, together  
150 with the simulations to the highest pressure of 25 GPa, allow the static compression mechanisms to  
151 be defined in more detail. The O-Si-O angles change by less than 1° over this entire pressure range,  
152 meaning that the distortion of the SiO<sub>4</sub> tetrahedra remains almost unchanged. However, the Si-O bond  
153 lengths shorten considerably, and the bulk modulus of the tetrahedra is 351(2) GPa. In contrast, the  
154 shorter Zr-O bonds are significantly softer than the longer Zr-O bonds, because the longer Zr-O bonds  
155 are to the oxygen atoms involved in the shared polyhedral edge with the SiO<sub>4</sub> tetrahedra, and are  
156 therefore stiffened by Zr-Si repulsion (Hazen and Finger 1979). The overall bulk modulus of the ZrO<sub>8</sub>  
157 polyhedra in zircon calculated from the DFT simulations is 209(1) GPa, so they are significantly  
158 softer than the SiO<sub>4</sub> tetrahedra.

159 The isothermal Reuss bulk modulus of zircon obtained from fitting a third-order Birch-Murnaghan  
160 equation of state (BM3 EoS) to the unit-cell volumes of the static DFT simulations (i.e. without zero-  
161 point vibrational effects) at high pressures is 220.3(5) GPa, indicating that the compression of the

162  $\text{ZrO}_8$  polyhedra dominate the bulk properties of zircon, with a  $K_0' = 4.71(4)$ . The bulk modulus is  
163 lower than the value of 227(2) GPa at 0 K that can be derived from a complete analysis of all available  
164 experimental data (Zaffiro et al. 2018). The pressure derivative of the bulk modulus,  $K_0'$ , cannot be  
165 reliably determined from currently-available experimental data, and has been estimated to lie in the  
166 range 5 to 6.5 at 300 K (Zaffiro et al. 2018). The DFT simulations reproduce the correct sense of  
167 elastic anisotropy (Table 1) known from experimental data (Ozkan and Jamieson 1978, Zaffiro et al.  
168 2018) with the *c*-axis being significantly stiffer under compression than the *a*-axis as a consequence  
169 of the chains of edge-sharing of the  $\text{SiO}_4$  and  $\text{ZrO}_8$  polyhedra that run parallel to the *c*-axis .

170

### 171 **Raman vibrational frequencies of zircon**

172 The experimental Raman shifts at 70 K reported by Syme et al. (1977) show a good agreement with  
173 the Raman active modes calculated at zero pressure and 0 K (Table 2). The calculated trends of the  
174 Raman shifts with pressure are in good agreement with recent experimental data up to 10 GPa  
175 obtained from non-metamict single crystals under hydrostatic pressure (Pina-Binvinat et al. 2018).  
176 That experimental study also confirmed that zircon does not undergo any phase transition under  
177 hydrostatic pressures up to 10 GPa at room temperature. The wavenumbers of most of the Raman  
178 modes are predicted to increase with increasing pressure, meaning that  $\partial\omega/\partial P$  is positive (Table 2),  
179 in agreement with the experimental data. As expected, bond lengths decrease as pressure (evaluated  
180 at the static level) is imposed on the crystal and this also changes the energetics of the crystal: the  
181 shortening of the interatomic distances increases the energy of the structure at the static equilibrium  
182 and also the restoring forces on the atoms, and therefore the vibrational frequencies. However, two  
183 Raman-active modes of zircon ( $E_{g1}(1)$  at  $\omega_{\text{DFT}} = 197 \text{ cm}^{-1}$  and  $B_{2g}$  at  $\omega_{\text{DFT}} = 250 \text{ cm}^{-1}$ ), show the  
184 opposite behavior, with softening of the vibrational frequency with increasing pressure. This is also  
185 in agreement with the experiments as shown in Figure 3 and Table 2.

186 As displayed in the animated sketches of the vibrations of these two modes shown in Figures S1 and  
187 S2 (see also Sheremetyeva et al. 2018), the specific atom displacements involved in these two modes  
188 are mainly *rigid* movements of the polyhedra which do not significantly modify the bond lengths. In

189 the  $B_{2g}$  mode the  $Zr^{4+}$  ions do not move appreciably, while the  $SiO_4$  units undergo a shearing motion  
190 that does not significantly modify the bond lengths. Similarly the  $E_g(1)$  mode consists of a *rigid*  
191 rotation around the  $c$ -axis of the  $SiO_4$  without changes in the Si–O bond lengths. In both cases, the  
192 application of external hydrostatic pressure slightly reduces the force constants, resulting in a  
193 lowering of the normal mode wavenumber with a negative  $\partial\omega/\partial P$  coefficient. In other words, the  
194 increase of the repulsion among the nuclei due to the volume contraction is dynamically partially  
195 compensated by the low-frequency  $SiO_4$ -rotation modes, which facilitate the reduction of the Si-O-  
196 Si bond angles and the increase of internuclear distances of the static equilibrium configuration (see  
197 the discussion in Prencipe et al. (2011)). As a consequence, the potential wells become shallower and  
198 the corresponding vibrational frequencies decrease as pressure increases.

199

200 In Table 2 we also report  $\partial\omega/\partial P$  from our simulations up to 25 GPa, which shows that  $\partial\omega/\partial P$  becomes  
201 more negative as pressure increases. However, none of the calculated frequencies of the Raman-active  
202 modes goes to zero, so this softening does not imply that the structure becomes dynamically unstable.  
203 Nonetheless our calculations show that the lowest-frequency mode at  $131\text{ cm}^{-1}$ , which is a silent mode  
204 with  $B_{1u}$  symmetry and thus not observable with conventional experimental Raman spectroscopy,  
205 softens completely to zero at around 20 GPa (Figure 4). Therefore, according to our calculations, if  
206 hydrostatic pressure conditions are maintained up to 20 GPa at 0 K zircon undergoes a displacive  
207 phase transition. This phenomenon was already reported by Smirnov et al. (2008) in DFT simulations  
208 of zircon up to 70 GPa, but the issue was not further discussed.

209

### 210 **High-Pressure – low-symmetry new polymorph**

211 Following the procedure used in Prencipe et al. (2011), the soft mode was analyzed by initially  
212 shifting the atoms of the unit cell along the eigenvector associated with the  $B_{1u}$  mode:  $I\bar{4}2d$  space  
213 group symmetry resulted. By optimizing the geometry in this space group and keeping the cell volume  
214 fixed at the value corresponding to the softening ( $P = 20\text{ GPa}$  and  $V = 246.05\text{Å}^3$ ), the optimised



215 structure has a static energy lower than the one resulting from the optimization at the same cell  
216 volumes but in the  $I4_1/amd$  space group. Therefore, the new polymorph can be described as a high-  
217 pressure – low symmetry zircon (HPLS  $ZrSiO_4$ ), with a space group  $I\bar{4}2d$  that is a direct subgroup  
218 of the space group  $I4_1/amd$  of zircon. After re-optimization, the structure does not show any drastic  
219 structural reconstruction but subtle structural differences which break the symmetry of zircon. The  
220 new phase has very similar unit-cell parameters,  $a = 6.399 \text{ \AA}$ ,  $c = 5.881 \text{ \AA}$  at  $P = 25 \text{ GPa}$ , compared  
221 to values for zircon constrained to the higher symmetry at the same pressure, of  $a = 6.426 \text{ \AA}$ ,  $c =$   
222  $5.890 \text{ \AA}$ . Because the transition is driven by a soft mode and is displacive in character, the structural  
223 topology of the new polymorph is the same as that of zircon, containing  $SiO_4$  tetrahedra and  $ZrO_8$   
224 dodecahedra, linked in the same way, so it is almost indistinguishable from zircon when viewed in  
225 the same orientation as zircon in Figure 1. Compared to zircon, all of the atoms of the high-pressure  
226 phase occupy Wyckoff positions of lower symmetry, and the  $\bar{4}$  symmetry of the Si position which is  
227  $\bar{4}m2$  in zircon allows the tetrahedra to be rotated compared to the fixed orientation in zircon. This is  
228 most obvious when the two structures are viewed down the  $c$ -axis (Figure 5). The oxygen atom  
229 therefore is no longer required to occupy a position on a  $\{100\}$  mirror plane (as in zircon) but occupies  
230 an unconstrained general equivalent position within the new polymorph. Comparison of the structures  
231 of zircon (constrained to  $I4_1/amd$  symmetry) and the relaxed structure of the new polymorph obtained  
232 from DFT simulations at the same pressures above the transition show that the individual bond  
233 lengths, O-Si-O angles, and O-O distances within the  $SiO_4$  tetrahedra are identical within the  
234 uncertainties in the simulations. Therefore, the mechanism of the transition is one of rotation of the  
235  $SiO_4$  tetrahedra around the  $c$ -axis of the structure, which is the same distortion that is generated by  
236 the soft  $B_{1u}$  mode within the zircon structure (Figure 5). This rotation alone, without any other  
237 distortion, leads to a reduction of the  $a$  and  $b$  cell parameters, a slight reduction in volume, and no  
238 change in the  $c$  cell parameter. The simulated structures of the new polymorph however also show a  
239 small reduction in the  $c$  cell parameter compared to zircon, which is due to small changes in the  
240 distortion of the  $ZrO_8$  dodecahedra. At 25 GPa, the new phase is 1% denser than zircon.

241 In summary, this phase transition is allowed by symmetry to be continuous in nature, and above 20  
242 GPa the spontaneous volume change (the volume difference between the HPLS phase and zircon at  
243 the same pressure) as well as the cosine of the tetrahedral rotation angle (Figure 5) evolve linearly  
244 with pressure, which would be consistent with the transition being second-order in character (in the  
245 Landau sense e.g. Carpenter et al. 1998). The wavenumber of the  $B_{1u}$  mode in zircon extrapolates to  
246 zero at ca. 19.5 GPa, and at 20 GPa it becomes imaginary, showing that the zircon structure becomes  
247 dynamically unstable between 19.5 and 20 GPa (Figure 4). A simulation of the HPLS polymorph at  
248 20 GPa confirms this; the tetrahedral rotation angle is  $5.2^\circ$  (clearly visible in Figure 5), and at higher  
249 pressures the tetrahedral rotation angle continues to increase. The phonon frequencies of the new  
250 structure under hydrostatic pressures up to 30 GPa remain positive, showing that it remains  
251 dynamically stable and does not undergo any further displacive-type phase transitions in this pressure  
252 range (Figure 4). A similar behavior is seen for the Raman-active mode at  $40\text{ cm}^{-1}$  in the high-  
253 symmetry phase of  $\text{Pb}_3(\text{PO}_4)_2$  under high pressure (Mihailova et al. 2015). However, linear  
254 extrapolation of the volume strain of the HPLS phase to zero would suggest instead that the transition  
255 occurs not at 19.5 GPa but at a static pressure of 16.5 - 17 GPa in our simulations, which then appears  
256 to indicate that the transition has a small  $\Delta V$  step of 0.4% between 19.5 and 20 GPa. This apparent  
257 discrepancy with the character of the phase transition may be due to the difficulties within DFT of  
258 simulating small distortions of the structure near to the phase transition. We also note that the  
259 simulations are performed at static pressures and the true character and the transition pressure may  
260 be slightly different in zircon at finite temperatures. Only experimental data could resolve this  
261 question.

262

263

264 **Reidite structure and elasticity**

265 The only published experimental structure of reidite was based on a low-resolution powder diffraction  
266 measurement sample recovered from a high-pressure experiment (Kusaba et al. 1986); several  
267 computer simulations have subsequently confirmed the stability and structure type (Marqués et al.  
268 2006, Smirnov et al. 2010, Dutta and Mandal 2012b, Du et al. 2012). Reidite has the scheelite  
269 structure type (Kusaba et al. 1986), and contains SiO<sub>4</sub> tetrahedra linked only by corners to the 3-  
270 dimensional framework of edge-sharing ZrO<sub>8</sub> dodecahedra. In our DFT simulation at static  
271 equilibrium, the SiO<sub>4</sub> tetrahedra have significantly longer bond lengths than in zircon (1.660 Å  
272 compared to 1.634 Å), and the tetrahedra are flattened along the *c*-axis compared to those in zircon,  
273 where the elongation along the *c*-axis is due to the sharing of the tetrahedral edges with ZrO<sub>8</sub> (see  
274 Figure 1b and Figure 2).

275 The simulations show that the SiO<sub>4</sub> tetrahedra in reidite have a bulk modulus of 436 GPa, slightly  
276 stiffer than in zircon up to 17 GPa, and that the ZrO<sub>8</sub> polyhedra are very similar in bulk  
277 compressibility to those in zircon (as for zircon, the results for reidite are from fits to static DFT  
278 simulations without zero-point vibrational effects). In contrast to zircon, the *longer* of the two  
279 symmetry-independent Zr-O bonds in reidite compresses significantly more than the *shorter* Zr-O  
280 bond, which is a more normal behaviour, and confirms the inferred influence of the shared O-O edges  
281 between the ZrO<sub>8</sub> and SiO<sub>4</sub> groups and the consequent Zr-Si repulsion on the anisotropy of  
282 compression of zircon (Hazen and Finger 1979). The direction of the elastic anisotropy is reversed in  
283 reidite with respect to zircon, with the compressional modulus of the *c*-axis of reidite (501(1) GPa)  
284 being similar to the *a*-axis of zircon (551(2) GPa). The bulk modulus for reidite is determined to be  
285 241(5) GPa (with  $K_0' = 4.7(6)$ , Table 1), which is about 9% stiffer than zircon and consistent with the  
286 9% density increase from zircon to reidite, as also estimated in previous DFT simulations (Marqués  
287 et al. 2006, Smirnov et al. 2008 Du et al. 2012, Dutta and Mandal 2012b). The experimental bulk  
288 modulus of reidite was reported to be  $301.4 \pm 11.5$  GPa (Scott et al. 2002) and 392 GPa (Ono et al.  
289 2004a), but the latter is based on only six data points without a measurement of the recovered sample.

290

291 The calculated wavenumbers of the Raman active modes (Table 3) are in very good agreement with  
292 the data reported by Gucsik (2007). The  $\partial\omega/\partial P$  slopes are all positive and thus all of the mode  
293 frequencies remain positive in the investigated pressure range, meaning that reidite remains  
294 dynamically stable. The modes that are more sensitive to pressure are those at higher wavenumbers,  
295 which are related to the symmetric and antisymmetric stretching of the  $\text{SiO}_4$ . Moreover, the DFT  
296 simulations show that the doublet  $B_g(3)$  and  $E_g(3)$  that is present at  $P = 0$  converges to a singlet at  
297 ca. 7 GPa.

### 298 **Zircon-Reidite transition**

299 The space group of reidite,  $I4_1/a$ , which is obviously a sub-group of the space group of zircon,  
300  $I4_1/amd$ , when referred to the same unit-cell and orientation led several authors to assume that reidite  
301 (and scheelite structures in general) is a distorted form of the zircon structure and can be obtained by  
302 a displacive-type distortion of the zircon structure (e.g. Kusaba et al. 1986, Knittle and Williams  
303 1993, Liu 1979; Glass and Liu 2001). This is not correct because the orientation of the symmetry  
304 elements with respect to the structural elements is different in the two phases. Structurally, the unit  
305 cell of reidite is rotated  $45^\circ$  around the  $c$ -axis with respect to that of zircon (Figure 1), and the  
306 relationship between the unit-cell parameters is  $a_r \sim a_z \sqrt{2}$ . This means that the directions of  
307 translation of the  $a$  glides in reidite and zircon are also at  $45^\circ$  to one another. The space group of  
308 zircon,  $I4_1/amd$ , does not contain  $a$ -glides with translations in the direction of the glides in reidite.  
309 Similarly, the (very approximate) doubling of the  $c$ -lattice parameter on going from zircon to reidite  
310 means that the elements of the  $4_1$  symmetry operator in reidite are not present in zircon. The  
311 consequence of this symmetry relationship is that the topology of the polyhedral linkages in the  
312 structures of zircon and reidite are different, and this difference is the major cause for the large density  
313 and volume contrast between the two phases. Because the  $\text{SiO}_4$  tetrahedra in zircon share two edges  
314 with the  $\text{ZrO}_8$  dodecahedra, each silicon atom has six zircon atoms in its secondary coordination  
315 (Figure 2). In the room pressure simulation, two Zr are at a distance of 3.01 Å from Si across the  
316 shared edges, and four at a distance of 3.65 Å. The average Si-Zr distance is 3.44 Å. In reidite, there

317 is only corner-sharing between the  $\text{SiO}_4$  and  $\text{ZrO}_8$  polyhedra, with each oxygen bonded to one Si, and  
318 two Zr. Each Si atom in the structure of reidite therefore has 8 Zr neighbours, four at 3.37 Å and four  
319 at 3.56 Å at room pressure. The average Si-Zr distance in reidite, 3.46 Å is thus almost the same as in  
320 zircon, but the density of reidite is much greater because the secondary (Si to Zr) coordination has  
321 increased from 6 to 8 (see Figure 1).

322 Consequently, zircon undergoes a significant structural rearrangement when it transforms to its high-  
323 pressure polymorph reidite. The transformation is reconstructive and will occur only when a  
324 substantial energy barrier is overcome, either by high-temperature or significant over-stepping of the  
325 boundary in pressure, or a combination of the two. Calculation of the enthalpies  $H = U + PV$  of the  
326 two polymorphs by combining the internal energy  $U$ , pressure  $P$  and volume  $V$  from the DFT  
327 simulations, shows that reidite becomes energetically more stable than zircon above a pressure of  
328 9.13(1) GPa (Figure 6) at 0 K. This is not dissimilar to experiments. The experimental Clapeyron  
329 slope (Ono et al. 2004b)  $\partial P/\partial T$  is zero or slightly positive, and extrapolation of the experimental  
330 results to 0 K would place the phase transition pressure between 6 and 8 GPa.

331

332

## IMPLICATIONS

333 The DFT simulations can now explain the various experimental data on zircon and its transformations  
334 at high pressure. The calculated  $P$ - $V$  curve from DFT is in good agreement with the data reported by  
335 Ono et al. (2004a) on quenched synthetic reidite samples as well as the results from the in-situ high-  
336 pressure study of zircon by van Westrenen et al. (2004) (Figure 7). The deviation to lower volumes  
337 seen above 19.7 GPa in the data of van Westrenen et al. (2004) are now seen to be the consequence  
338 of the displacive phase transition to the new HPLS zircon phase that we have discovered in this DFT  
339 study. Raman spectra of the recovered sample from this experiment unequivocally show reidite so  
340 this suggests that, due to the sluggish character of the zircon to reidite transition, at high pressures the  
341 sample actually contained HPLS zircon plus an amount of reidite too small to be detected by  
342 diffraction. This shows that compression at room temperature and above 20 GPa is sufficient to

343 overcome the activation barrier for the zircon to reidite transformation, and that at high pressures the  
344 sample will consist of a mixture of the HPLS zircon phase which has partially transformed to reidite.  
345 On pressure release the HPLS zircon will transform back to normal zircon, while the reidite may not,  
346 so that recovered samples consist of a mixture of reidite and zircon.

347 The DFT simulations of the Raman spectra of all three polymorphs allow us to give some guidelines  
348 as to which peaks in experimental Raman spectra are diagnostic for the different phases of  $\text{ZrSiO}_4$ .  
349 The simulation of zircon at high pressure (e.g. 19.5 GP) shows that peaks shifts toward higher  
350 wavenumbers (Figure 8), while the mode  $E_g(1)$  shifts to lower wavenumbers under pressure, as we  
351 discussed in detail above. Above ca. 20 GPa zircon is no longer stable and the symmetry is broken,  
352 resulting in the HPLS phase. At 20 GPa, according to the irreducible representations of point groups  
353 (for the  $\Gamma$  point) the  $B_{1u}$  mode which is silent for the  $4/mmm$  point group of zircon, turns into an  $A_1$   
354 symmetry mode for the  $\bar{4}2m$  point group symmetry of the HPLS phase, which is Raman active. This  
355 mode has a high intensity even with random polarization as shown in Figure 8 and occurs at  $94 \text{ cm}^{-1}$   
356 at  $P = 20 \text{ GPa}$ . Tables S1 – S3 list the relative intensities of the Raman peaks of all three polymorphs  
357 simulated for single crystals and polycrystalline powders. Therefore, the HPLS phase can be  
358 distinguished from zircon in-situ in high-pressure experiments by making Raman measurements in  
359 the low wavenumbers range (below  $200 \text{ cm}^{-1}$ ), where the peak at  $94 \text{ cm}^{-1}$  does not overlap with any  
360 peaks of reidite or zircon.

361

362

363

## Acknowledgments

364 This work was supported by ERC starting grant 714936 ‘True Depths’, the Italian Ministry for  
365 Research and University (MIUR) SIR grant “MILE DEEP” (RBSI140351) and the MIUR FARE  
366 research grant R164WEJAHH, all to Matteo Alvaro. We thank Wim van Westrenen and an  
367 anonymous reviewer for their comments on the manuscript.

368

369

## References

370

371 Aliatis, I., Lambruschi, E., Mantovani, L., Bersani, D., Andò, S., Diego Gatta, G., Gentile, P.,  
372 Salvioli-Mariani, E., Prencipe, M., Tribaudino, M., Lottici, P.P. (2015) A comparison between  
373 ab initio calculated and measured Raman spectrum of triclinic albite ( $\text{NaAlSi}_3\text{O}_8$ ). *Journal of*  
374 *Raman Spectroscopy*, 46, 501–508.

375 Angel, R.J., Gonzalez-Platas, J., and Alvaro, M. (2014) EosFit7c and a Fortran module (library) for  
376 equation of state calculations. *Zeitschrift für Kristallographie*, 229, 405–419.

377 Carpenter, M.A., Salje, E.K.H., and Graeme-Barber, A. (1998) Spontaneous strain as a determinant  
378 of thermodynamic properties for phase transitions in minerals. *European Journal of Mineralogy*,  
379 10, 621–691.

380 Cavosie, A.J., Erickson, T.M., and Timms, N.E. (2015) Nanoscale records of ancient shock  
381 deformation: reidite ( $\text{ZrSiO}_4$ ) in sandstone at the Ordovician Rock Elm impact crater. *Geology*,  
382 43, 315–318.

383 Cavosie, A.J., Timms, N.E., Erickson, T.M., and Koeberl, C. (2018) New clues from Earth’s most  
384 elusive impact crater: evidence of reidite in Australasian tektites from Thailand. *Geology*, 46,  
385 203–206.

386 Chen, M., Yin, F., Li, X., Xie, X., Xiao, W., and Tan, D. (2013) Natural occurrence of reidite in the  
387 Xiuyan crater of China. *Meteoritics & Planetary Science*, 48, 796–805.

388 Civalleri, B., D’Arco, P., Orlando, R., Saunders, V.R., and Dovesi, R. (2001) Hartree–Fock geometry

- 389 optimisation of periodic systems with the crystal code. *Chemical Physics Letters*, 348, 131-138.
- 390 Cremer, D. (2001) Density functional theory: coverage of dynamic and non-dynamic electron  
391 correlation effects. *Molecular Physics*, 99, 1899–1940.
- 392 CrystalMaker (2018): CrystalMaker, a crystal & molecular structures modelling program for Mac &  
393 Windows, [www.crystallmaker.com](http://www.crystallmaker.com). CrystalMaker Software Ltd, Oxford, U.K.
- 394 Doll, K., Saunders, V.R., and Harrison, N.M. (2001) Analytical Hartree-Fock gradients for periodic  
395 systems. *International Journal of Quantum Chemistry*, 82, 1–31.
- 396 Dovesi, R., Orlando, R., Erba, A., Zicovich-Wilson, C.M., Civalleri, B., Casassa, S., Maschio, L.,  
397 Ferrabone, M., De La Pierre, M., D'Arco, P., Noel, Y., Causà, M., Rérat, M., Kirtman, B. (2014)  
398 CRYSTAL14: A program for the ab initio investigation of crystalline solids. *International*  
399 *Journal of Quantum Chemistry*, 114, 1287–1317.
- 400 Dovesi, R., Erba, A., Orlando, R., Zicovich-Wilson, C.M., Civalleri, B., Maschio, L., Rérat, M.,  
401 Casassa, S., Baima, J., Salustro, S., Kirtman, B., (2018) Quantum-mechanical condensed matter  
402 simulations with CRYSTAL. *Wiley Interdisciplinary Reviews: Computational Molecular*  
403 *Science*, e1360.
- 404 Du, J., Devanathan, R., René Corrales, L., and Weber, W.J. (2012) First-principles calculations of the  
405 electronic structure, phase transition and properties of ZrSiO<sub>4</sub> polymorphs. *Computational and*  
406 *Theoretical Chemistry*, 987, 62–70.
- 407 Dutta, R., and Mandal, N. (2012a) Effects of pressure on the elasticity and stability of zircon (ZrSiO<sub>4</sub>):  
408 First-principle investigations. *Computational Materials Science*, 54, 157–164.
- 409 Dutta, R., and Mandal, N. (2012b) Structure, elasticity and stability of reidite (ZrSiO<sub>4</sub>) under  
410 hydrostatic pressure: A density functional study. *Materials Chemistry and Physics*, 135, 322–  
411 329.
- 412 Ferrero, M., Rérat, M., Orlando, R., Dovesi, R., and Bush, I.J. (2008) Coupled perturbed Kohn-Sham  
413 calculation of static polarizabilities of periodic compounds. In *Journal of Physics: Conference*  
414 *Series Vol. 117*, p. 012016. IOP Publishing.
- 415 Finch, R.J. and Hanchar, J.M. (2003) Structure and chemistry of zircon and zircon-group minerals.



- 416       Reviews in Mineralogy and Geochemistry, 53, 1–25.
- 417   Finch, R.J., Hanchar, J.M., Hoskin, P.W.O., and Burns, P.C. (2001) Rare-earth elements in synthetic  
418       zircon: Part 2. A single-crystal X-ray study of xenotime substitution. *American Mineralogist*,  
419       86, 681–689.
- 420   French, B.M. (1998) Traces of catastrophe: A handbook of shock-metamorphic effects in terrestrial  
421       meteorite impact structures, LPI Contribution, 954 p.
- 422   French, B.M., and Koeberl, C. (2010) The convincing identification of terrestrial meteorite impact  
423       structures: What works, what doesn't, and why. *Earth-Science Reviews*, 98, 123–170.
- 424   Glass, B.P., and Liu, S. (2001) Discovery of high-pressure ZrSiO<sub>4</sub> polymorph in naturally occurring  
425       shock-metamorphosed zircons. *Geology*, 29, 371–373.
- 426   Glass, B.P., Liu, S., and Leavens, P.B. (2002) Reidite: An impact-produced high-pressure polymorph  
427       of zircon found in marine sediments. *American Mineralogist*, 87, 562–565.
- 428   Gucsik, A. (2007) Micro-Raman spectroscopy of reidite as an impact-induced high pressure  
429       polymorph of zircon: experimental investigation and attempt to application. *Acta Mineralogica*  
430       Petrographica, 47, 17–24.
- 431   Gucsik, A., Zhang, M., Koeberl, C., Salje, E.K.H., Redfern, S.A.T., and Pruneda, J.M. (2004) Infrared  
432       and Raman spectra of ZrSiO<sub>4</sub> experimentally shocked at high pressures. *Mineralogical*  
433       Magazine, 68, 801–811.
- 434   Hazen, R.M., and Finger, L.M. (1979) Crystal structure and compressibility of zircon at high pressure.  
435       *American Mineralogist*, 64, 196–201.
- 436   Knittle, E., and Williams, Q. (1993) High-pressure Raman spectroscopy of ZrSiO<sub>4</sub>: observation of  
437       the zircon to scheelite transition at 300 K. *American Mineralogist*, 78, 245–252.
- 438   Kolesov, B.A., Geiger, C.A., and Armbruster, T. (2001) The dynamic properties of zircon studied by  
439       single-crystal X-ray diffraction and Raman spectroscopy. *European Journal of Mineralogy*, 13,  
440       939–948.
- 441   Kusaba, K., Yag, T., Kikuchi, M., and Syono, Y. (1986) Structural considerations on the mechanism  
442       of the shock-induced zircon-scheelite transition in ZrSiO<sub>4</sub>. *Journal of Physics and Chemistry of*

- 443 Solids, 47, 675.
- 444 Langenhorst, F., and Deutsch, A. (2012) Shock metamorphism of minerals. *Elements*, 8, 31–36.
- 445 Lee, C.T., Yang, W.T., and Parr, R.G. (1988) Development of the Colle-Salvetti correlation-energy  
446 formula into a functional of the electron-density. *Physical Review B*, 37, 785–789.
- 447 Leroux, H., Reimold, W.U., Koeberl, C., Hornemann, U., and Doukhan, J.C. (1999) Experimental  
448 shock deformation in zircon: a transmission electron microscopic study. *Earth and Planetary  
449 Science Letters*, 169, 291–301.
- 450 Liu, L.G. (1979) High-pressure phase transformations in baddeleyite and zircon, with geophysical  
451 implications. *Earth and Planetary Science Letters*, 44, 390–396.
- 452 Marqués, M., Flórez, M., Recio, J.M., Gerward, L., and Olsen, J.S. (2006) Structure and stability of  
453  $ZrSiO_4$  under hydrostatic pressure. *Physical Review B - Condensed Matter and Materials  
454 Physics*, 74, 1–9.
- 455 Maschio, L., Kirtman, B., Salustro, S., Zicovich-Wilson, C.M., Orlando, R., and Dovesi, R. (2013)  
456 Raman spectrum of pyrope garnet. A quantum mechanical simulation of frequencies, intensities,  
457 and isotope shifts. *Journal of Physical Chemistry A*, 117, 11464–11471.
- 458 Mihailova, B., Angel, R.J., Waesermann, N., Maier, B.J., Paulmann, C., and Bismayer, U. (2015)  
459 Pressure-induced transformation processes in ferroelastic  $Pb_3(P_{1-x}As_xO_4)_2$ ,  $x = 0$  and 0.80.  
460 *Zeitschrift für Kristallographie - Crystalline Materials*, 230, 593–603.
- 461 Morozova, I. (2015) Strength study of zircon under high pressure. Master Thesis, University of  
462 Western Ontario.
- 463 Ono, S., Tange, Y., Katayama, I., and Kikegawa, T. (2004a) Equations of state of  $ZrSiO_4$  phases in  
464 the upper mantle. *American Mineralogist*, 89, 185–188.
- 465 Ono, S., Funakoshi, K., Nakajima, Y., Tange, Y., and Katsura, T. (2004b) Phase transition of zircon  
466 at high P-T conditions. *Contributions to Mineralogy and Petrology*, 147, 505–509.
- 467 Ozkan, H., and Jamieson, J.C. (1978) Pressure dependence of the elastic constants of nonmetamict  
468 zircon. *Physics and Chemistry of Minerals*, 224, 215–224.
- 469 Pascale, F., Zicovich-Wilson, C.M., Lopez Gejo, F., Civalleri, B., Orlando, R., and Dovesi, R.T.

- 470 (2004) The calculation of the vibrational frequencies of crystalline compounds and its  
471 implementation in the CRYSTAL code. *Journal of Computational Chemistry*, 25, 888-897.
- 472 Pina-Binvignat, F.A., Malcherek, T., Angel, R.J., Paulmann, C., Schlüter, J., and Mihailova, B.  
473 (2018) Effect of radiation-induced structural damage on the structural response of zircon to high  
474 pressures. *Physics and Chemistry of Minerals*, 45, 981-993.
- 475 Prencipe, M. (2012) Simulation of vibrational spectra of crystals by ab initio calculations: An  
476 invaluable aid in the assignment and interpretation of the Raman signals. The case of jadeite  
477 (NaAlSi<sub>2</sub>O<sub>6</sub>). *Journal of Raman Spectroscopy*, 43, 1567–1569.
- 478 Prencipe, M., Scanavino, I., Nestola, F., and Merlini, M. (2011) High-pressure thermo-elastic  
479 properties of beryl (Al<sub>4</sub>Be<sub>6</sub>Si<sub>12</sub>O<sub>36</sub>) from ab initio calculations, and observations about the source  
480 of thermal expansion. *Physics and Chemistry of Minerals*, 38(3), 223-239.
- 481 Reddy, S.M., Johnson, T.E., Fischer, S., Rickard, W.D.A., and Taylor, R.J.M. (2015) Precambrian  
482 reidite discovered in shocked zircon from the Stac Fada impactite, Scotland. *Geology*, 43, 899–  
483 902.
- 484 Reid, A.F., and Ringwood, A.E. (1969) Newly observed high pressure transformations in Mn<sub>3</sub>O<sub>4</sub>,  
485 CaAl<sub>2</sub>O<sub>4</sub>, and ZrSiO<sub>4</sub>. *Earth and Planetary Science Letters*, 6, 205–208.
- 486 Scott, H.P., Williams, Q., and Knittle, E. (2002) Ultralow compressibility silicate without highly  
487 coordinated silicon. *Physical Review Letters*, 88, 015506.
- 488 Sheremetyeva, N., Cherniak, D.J., Watson, E.B., and Meunier, V. (2018) Effect of pressure on the  
489 Raman-active modes of zircon (ZrSiO<sub>4</sub>): a first-principles study. *Physics and Chemistry of*  
490 *Minerals*, 45, 173–184.
- 491 Singleton, A.C., Osinski, G.R., and Shieh, S.R. (2015) Microscopic effects of shock metamorphism  
492 in zircons from the Houghton impact structure, Canada. *Geological Society of America Special*  
493 *Papers*, 518, 135–148.
- 494 Smirnov, M.B., Mirgorodsky, A.P., Kazimirov, V.Y., and Guinebretière, R. (2008) Bond-switching  
495 mechanism for the zircon-scheelite phase transition. *Physical Review B - Condensed Matter and*  
496 *Materials Physics*, 78, 1–11.

- 497 Smirnov, M.B., Sukhomlinov, S. V., and Smirnov, K.S. (2010) Vibrational spectrum of reidite  $ZrSiO_4$   
498 from first principles. *Physical Review B*, 82, 094307.
- 499 Sophia, G., Baranek, P., Sarrazin, C., Rérat, M., and Dovesi, R. (2013) First-principles study of the  
500 mechanisms of the pressure-induced dielectric anomalies in ferroelectric perovskites. *Phase*  
501 *Transitions*, 86, 1069–1084.
- 502 Stangarone, C., Tribaudino, M., Prencipe, M., and Lottici, P.P. (2016) Raman modes in Pbcu enstatite  
503 ( $Mg_2Si_2O_6$ ): an assignment by quantum mechanical calculation to interpret experimental results.  
504 *Journal of Raman Spectroscopy*, 47, 1247–1258.
- 505 Stangarone, C., Böttger, U., Bersani, D., Tribaudino, M., and Prencipe, M. (2017) *Ab initio*  
506 simulations and experimental Raman spectra of  $Mg_2SiO_4$  forsterite to simulate Mars surface  
507 environmental conditions. *Journal of Raman Spectroscopy*, 48, 1528-1535
- 508 Syme, R.W.G., Lockwood, D.J., and Kerr, H.J. (1977) Raman spectrum of synthetic zircon ( $ZrSiO_4$ )  
509 and thorite ( $ThSiO_4$ ). *Journal of Physics C: Solid State Physics*, 10, 1335–1348.
- 510 Valenzano, L., Torres, F.J., Doll, K., Pascale, F., Zicovich-Wilson, C.M., and Dovesi, R. (2006) *Ab*  
511 *initio* study of the vibrational spectrum and related properties of crystalline compounds; the case  
512 of  $CaCO_3$  Calcite. *Zeitschrift für Physikalische Chemie*, 220, 893–912.
- 513 Van Westrenen, W., Frank, M.R., Hanchar, J.M., Fei, Y., Finch, R.J., and Zha, C.S. (2004) In situ  
514 determination of the compressibility of synthetic pure zircon ( $ZrSiO_4$ ) and the onset of the  
515 zircon-reidite phase transition. *American Mineralogist*, 89, 197–203.
- 516 Wittmann, A., and Reimold, W. (2009) The record of ground zero in the Chesapeake Bay impact  
517 crater—Suevites and related rocks. *GSA Special Paper*, 458, 349–376.
- 518 Wittmann, A., Kenkmann, T., Schmitt, R.T., and Stöffler, D. (2006) Shock-metamorphosed zircon in  
519 terrestrial impact craters. *Meteoritics and Planetary Science*, 41, 433–454.
- 520 Wu, Z., and Cohen, R.E. (2005) Generalized gradient approximation made more accurate for solids.  
521 *Physical Review B*, 73, 235116.
- 522 Zaffiro, G., Angel, R.J., Alvaro, M., Prencipe, M., and Stangarone, C. (2018) P-V-T-Ks Equations of  
523 state for zircon and rutile. *Geophysical Research Abstract*, Vol. 20, p. 6952.

525

## Tables

526 **Table 1.** Calculated zircon and reidite EoS parameters

	$V_0$ ( $\text{\AA}^3$ )	$K_0$ (GPa)	$K_0'$	$a_0$ ( $\text{\AA}$ )	$M_{a0}$ (GPa)	$M_{a0}'$	$c_0$ ( $\text{\AA}$ )	$M_{c0}$ (GPa)	$M_{c0}'$
<b>zircon</b>	266.49 (11)	220.3 (5)	4.71 (4)	6.6514 (2)	551 (2)	15.8 (2)	6.0238 (2)	1050 (1)	5.3 (2)
<b>reidite</b>	239.57 (6)	241 (5)	4.7 (6)	4.76078 (3)	921 (2)	10.1 (2)	10.5700 (2)	501 (1)	16.1 (2)

527

528 Note: Parameters are for Birch-Murnaghan 3<sup>rd</sup>-order EoS, obtained by fitting the unit-cell volumes

529 and cell parameters from the static DFT simulations up to 25 GPa for zircon, and to 17 GPa for reidite.

530

531 **Table 2.** Wavenumbers ( $\omega$ ) and their pressure derivatives ( $\partial\omega/\partial P$ ) of Raman-active modes of zircon

mode	$\omega$ (cm <sup>-1</sup> )		$\partial\omega/\partial P$ (cm <sup>-1</sup> /GPa)			
	Experimental <sup>a</sup>		experimental <sup>b</sup>		calculated	
	T = 70 K	0 K P = 0	T = 298 K P = 0	up to 10 GPa	up to 10 GPa	up to 25 GPa
<b>A<sub>1g</sub> (1)</b>	441.5	439	439.6	1.44	1.50	1.37
<b>A<sub>1g</sub> (2)</b>	978	970	975.4	4.97	4.84	4.28
<b>B<sub>1g</sub> (1)</b>	216.5	216	215.1	1.27	1.37	1.12
<b>B<sub>1g</sub> (2)</b>	395	387	394.0	1.86	2.08	1.86
<b>B<sub>1g</sub> (3)</b>	642	636	–	–	2.05	1.82
<b>B<sub>1g</sub> (4)</b>	1012.5	1015	1008.6	5.54	5.23	4.61
<b>B<sub>2g</sub></b>	265	250	–	–	-1.33	-1.46
<b>E<sub>g</sub> (1)</b>	202.5	197	202.6	-0.56	-0.56	-0.81
<b>E<sub>g</sub> (2)</b>	225.5	225	224.5	0.30	0.05	0.07
<b>E<sub>g</sub> (3)</b>	360	341	357.9	4.27	4.57	3.92
<b>E<sub>g</sub> (4)</b>	547	542	–	–	0.71	0.63
<b>E<sub>g</sub> (5)</b>	927	922	–	–	4.89	4.32

532 <sup>a</sup>Syme et al. 1977

533 <sup>b</sup>Pinvignat et al. 2018

534

535 **Table 3.** Wavenumbers ( $\omega$ ) and their pressure derivatives ( $\partial\omega/\partial P$ ) of Raman-active modes of reidite

536

mode	Experimental <sup>a</sup>		calculated $\partial\omega/\partial P$
	T=298 K	T=0 K	
<b>Ag (1)</b>	327	326	1.05
<b>Ag (2)</b>	406	409	0.53
<b>Ag (3)</b>	-	861	1.29
<b>Bg (1)</b>	238	242	0.71
<b>Bg (2)</b>	353	350	2.70
<b>Bg (3)</b>	464	465	1.80
<b>Bg (4)</b>	610	608	2.19
<b>Bg (5)</b>	847	852	1.64
<b>Eg (1)</b>	205	209	2.05
<b>Eg (2)</b>	297	300	1.90
<b>Eg (3)</b>	-	458	4.18
<b>Eg (4)</b>	558	558	3.42
<b>Eg (5)</b>	887	891	4.51

537

538 Notes: <sup>a</sup> Gucsik 2007. Calculated slopes are from simulations up to a maximum pressure of 17 GPa

539

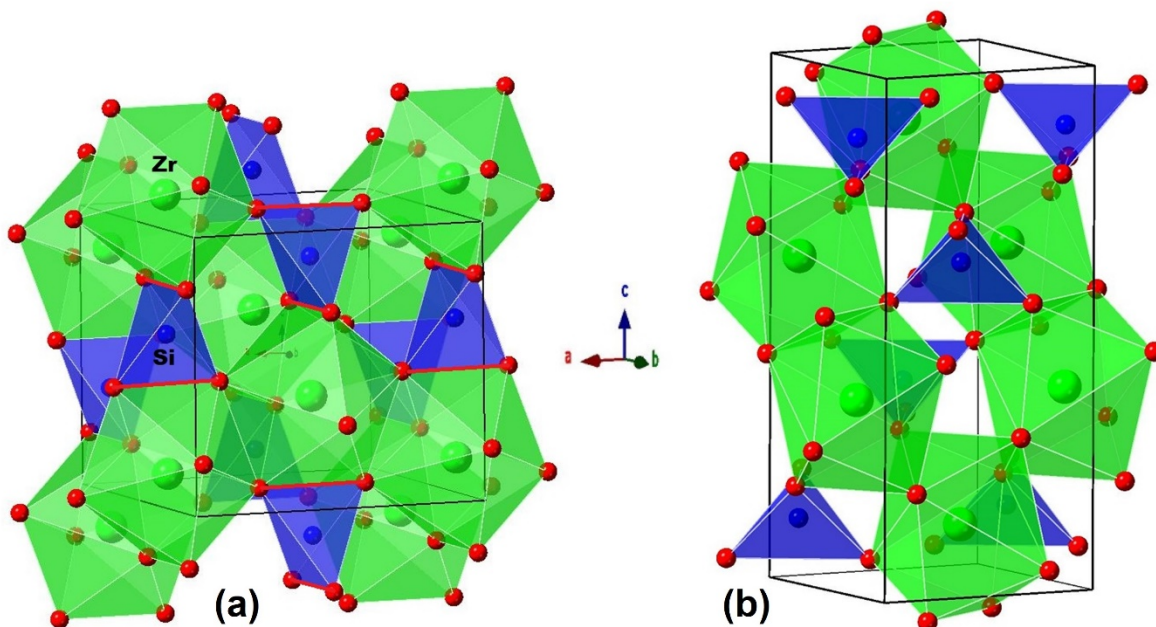
540

541

542

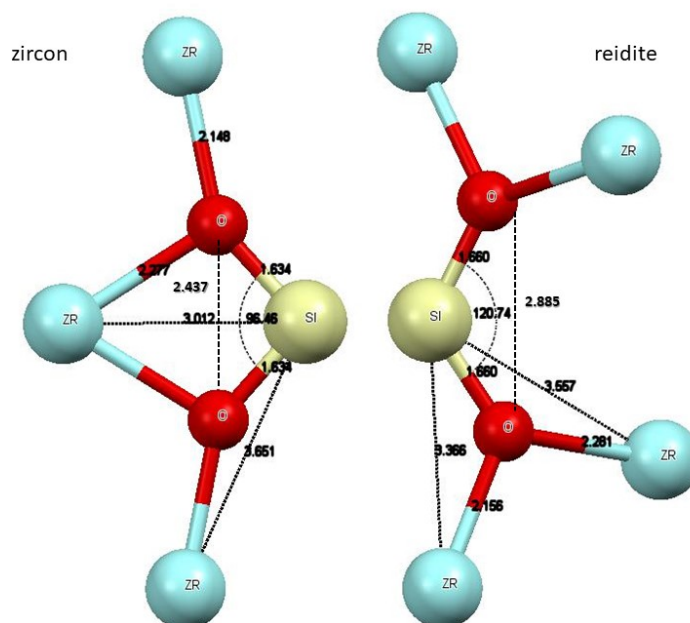
## Figures

543 **Figure 1.** Polyhedral representations of the crystal structures of (a) zircon and (b) reidite drawn with  
544 CrystalMaker® (2018). The shared O-O edges between the  $ZrO_8$  and the  $SiO_4$  polyhedra in zircon  
545 are highlighted in red.



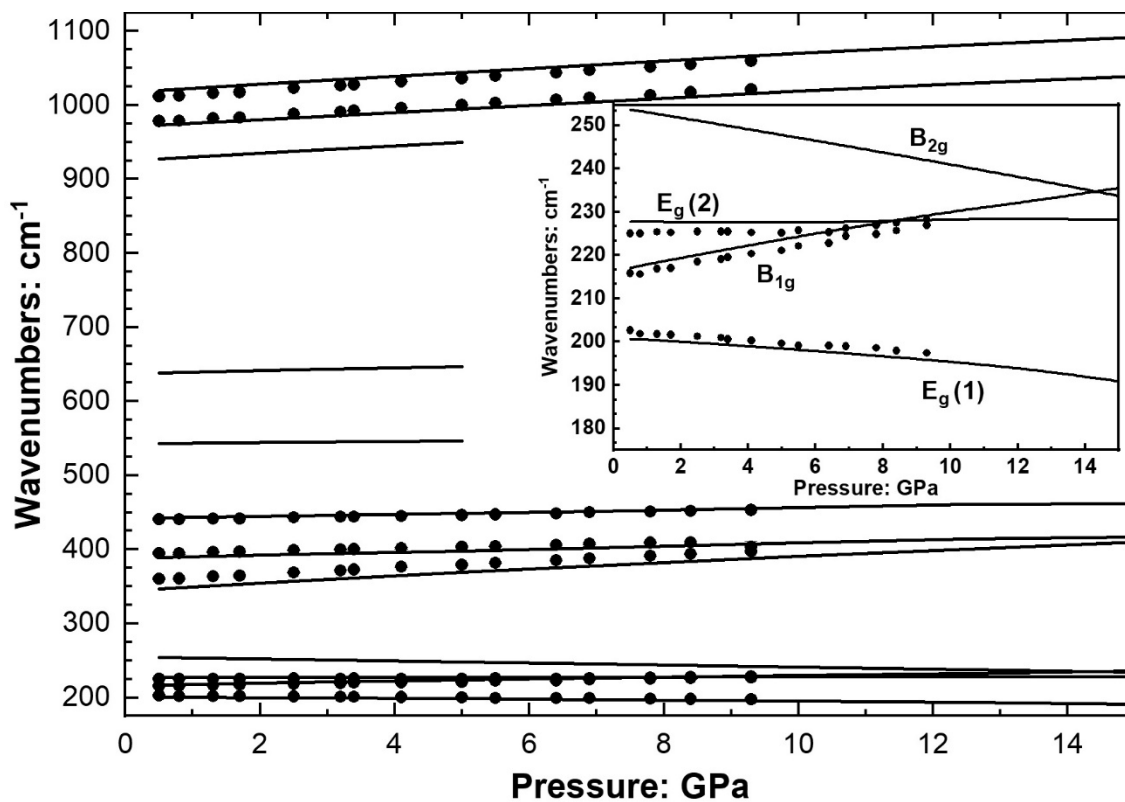
546

547 **Figure 2.** Interatomic distances (Å) and angles of zircon and reidite in the simulated structures at zero  
548 pressure. Only one-half of each  $SiO_4$  tetrahedron is shown for each polymorph. Note that in zircon  
549 two oxygens are shared by one Si and one Zr and form a shared polyhedral edge.





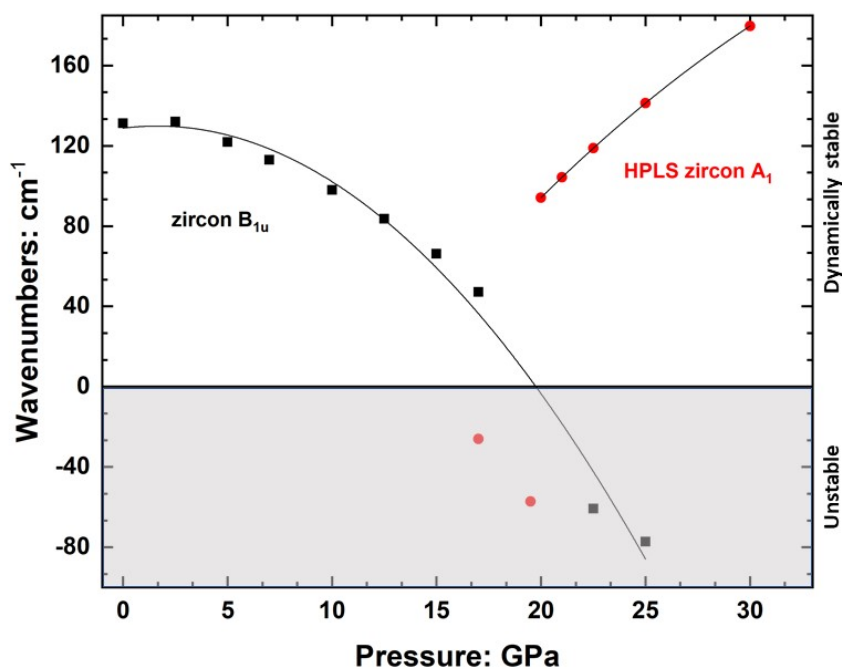
550 **Figure 3.** Calculated (lines) and experimental Raman shifts of zircon (Pina-Binvignat et al., 2018,  
551 symbols) as a function of pressure. Some of the calculated Raman active modes are not observed in  
552 experiments because of their low intensities. The inset shows the softening of the  $B_{2g}$  and  $E_g(1)$  modes  
553 with pressure.



554

555

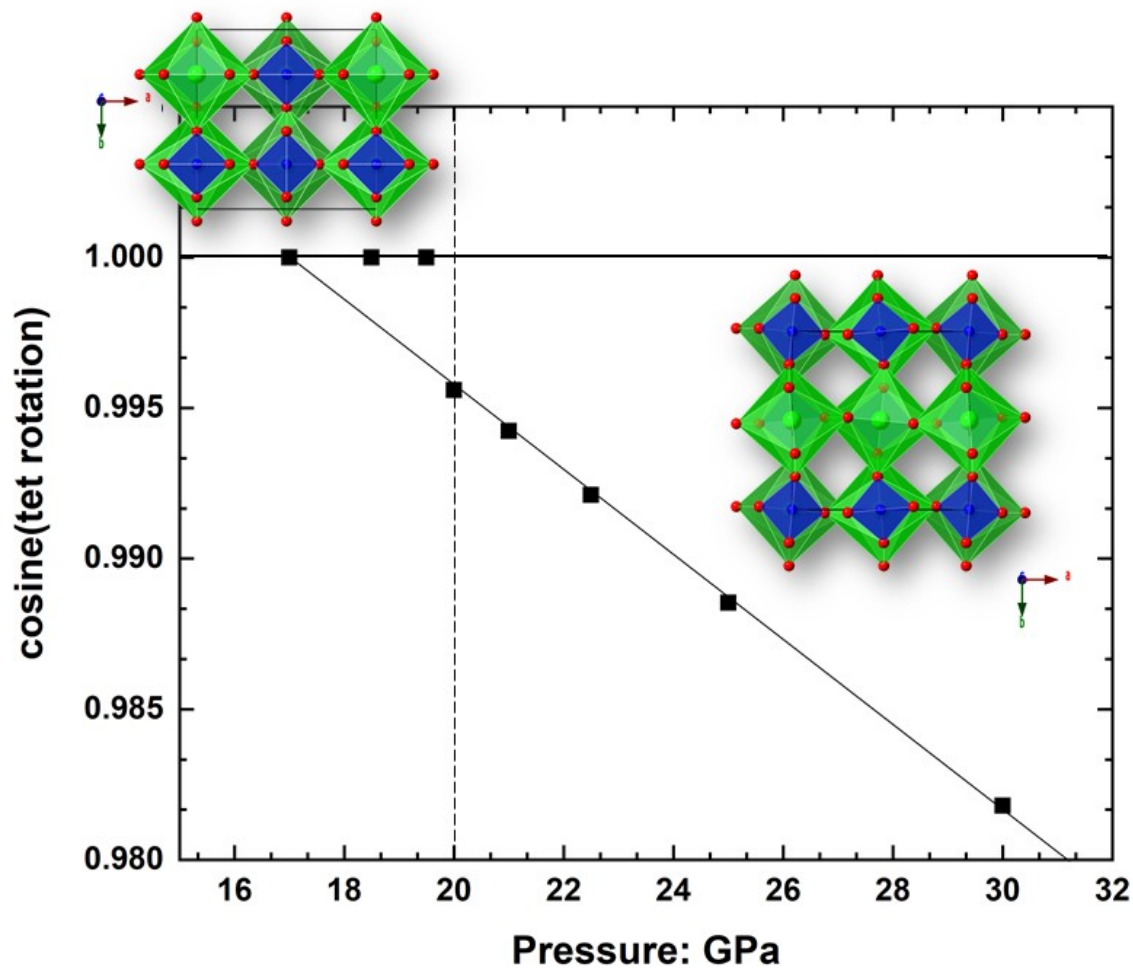
556 **Figure 4.** Variation of the wavenumber of the silent (i.e. neither Raman nor IR active)  $B_{1u}$  mode with  
557 pressure. Up to ca. 20 GPa the mode frequency is positive, but softens with pressure, and then  
558 becomes imaginary (plotted here as negative). In HPLS  $ZrSiO_4$  this mode becomes an  $A_1$  mode  
559 (circles).



560

561

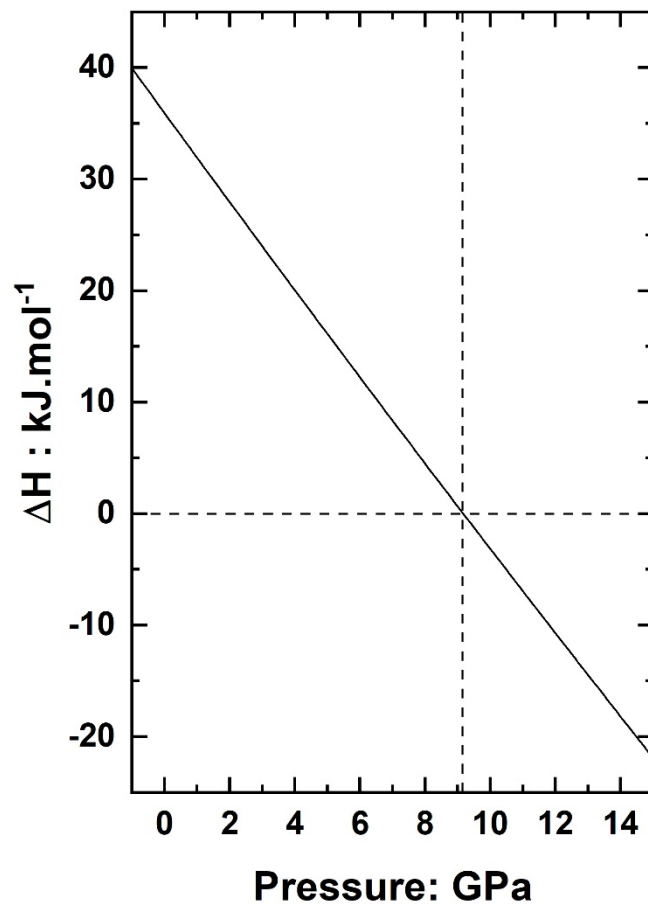
562 **Figure 5.** Variation with pressure of the cosine of the tetrahedral rotation angle, with polyhedral  
563 representations of (left) zircon and (right) HPLS zircon viewed down their *c*-axes. The tetrahedra are  
564 not rotated in zircon but become rotated in the HPLS phase.  
565



566

567

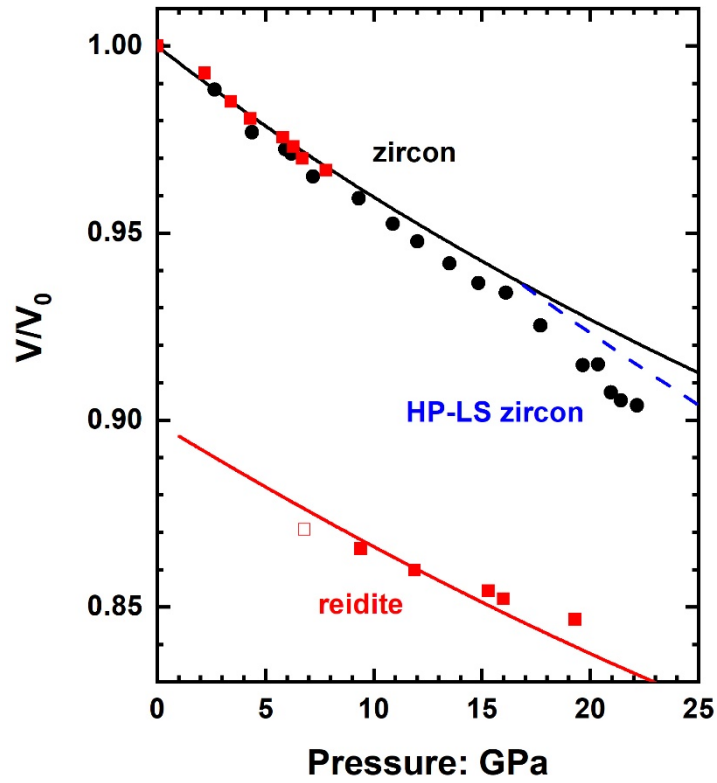
568 **Figure 6.** Variation of the enthalpy change  $\Delta H$  for the zircon to reidite transition with pressure  
569 calculated from DFT at 0 K, showing that the transition pressure is 9.13(1) GPa.



570

571

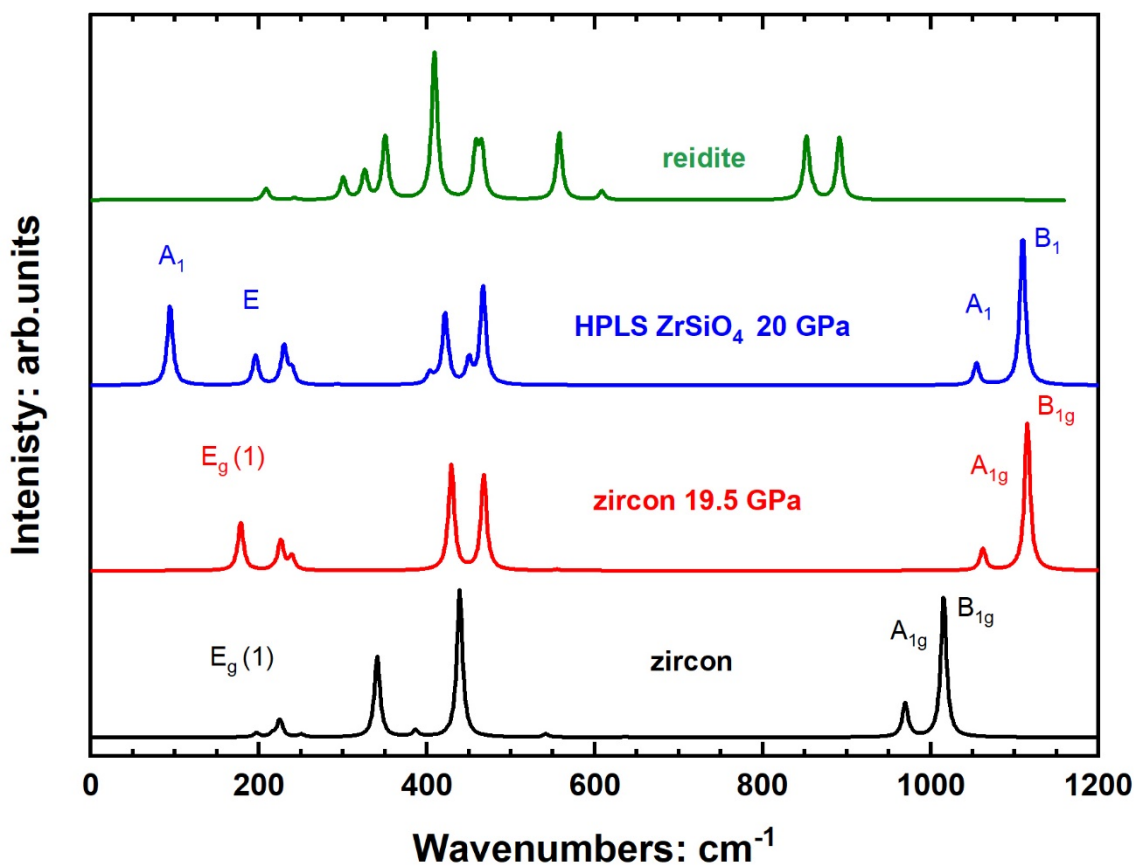
572 **Figure 7.**  $P$ - $V$  curves of the three polymorphs calculated by DFT at 0 K (lines) and experimental data  
573 at 300 K (red symbols Ono et al., 2004a; black symbols Van Westrenen, 2004). The deflection above  
574 19 GPa in the experimental data for zircon is in agreement with the smaller volume of the HPLS  
575 phase.



576

577

578 **Figure 8.** Calculated Raman spectra of the three polymorphs: the spectra are simulated for a  
579 polycrystalline powder without any polarization. The Raman intensities are calculated at 298 K and  
580 with a wavelength excitation of 532 nm. Calculated intensities for oriented single crystals in different  
581 scattering geometries are given in the supplementary materials Tables S1, S2 and S3.  
582



583

584